APPENDIX I

CONF-8707124--1

for the Neutron Resonance Radiography Workshop
July 27-29, 1987 Los Alamos National Laboratory

CONF-8707124--1

DE88 001715

NBS WORK ON NEUTRON RESONANCE RADIOGRAPHY

by R.A. Schrack

National Bureau of Standards

AI01-86ER11275

NBS has been engaged in a wide-ranging program in Neutron Resonance Radiography utilizing both one- and two-dimensional position-sensitive neutron detectors. The ability to perform a position-sensitive assay of up to 16 isotopes in a complex matrix has been demonstrated for a wide variety of sample types, including those with high gamma activity. A major part of the program has been the development and application of the microchannel-plate-based position-sensitive neutron detector. This detector system has high resolution and sensitivity, together with adequate speed of response to be used with neutron time-of-flight techniques. This system has demonstrated the ability to simultaneously image three isotopes in a sample with no interference.

jsw

NBS Work on Neutron Resonance Radiography

About ten years ago Charlie Bowman initiated a research program on NRR at NBS. The people involved in that program have been Jim Behrens, Charlie Bowman, Ron Johnson, and myself. I will review the work that has been done up to 1983, at which time the program ended.

The NBS Linac provides a barely adequate source of neutrons with pulse repetition rates from 30 to 720 pps into flight paths from 5 to 200 meters in length. Most of the work reported on today was done with flight paths of about 8 meters and pulse repetition rates of about 60 pps.

Very preliminary work was done with a spot-collimated beam and mechanical scanning. These early experiments were quickly followed by a system using a fan-shaped neutron beam and a He-3 linear position-sensitive proportional counter (PSPC). The sample was moved in one dimension as shown in figure 1. Figure 2 shows the experimental results obtained examining the silver distribution between a set of brazed washers. A defect in the brazing had been deliberately introduced. From an analysis of the shape of the 5.2 eV line of Ag-109, the amount of silver in each pixel area was determined. The pixel size in this picture is 3.2 x 3.0 mm. There are 25 x 26 pixels in the picture.

To obtain higher resolution, a small linear PSPC having a sensitive length of 50 mm and a spatial resolution of 1.2 mm was built in collaboration with M. K. Kopp of ORNL. Using this detector, an assay was made of the content of fresh nuclear fuel pellets. Because of the poor resolution, no attempt was made to do a position-sensitive assay, and an analysis was made on the grouped data of those pixels that included the pellet.

The time-of-flight transmission spectrum through the pellet shown in Figure 3 was analyzed using a non-linear fitting procedure that took into account the response function of the detector system. The results of the measurements of the mass ratio of U-235 to U-238 for high-enriched and low-enriched pellets are shown in Table I, as well as the values of the ratio determined by scintillation spectrometry supplied by the manufacturer.

The analysis technique was next applied to spent fuel. One sample was cut from the center of a fuel rod and one from the end of the fuel rod. The transmission spectra obtained for these samples are shown in figure 4. As with the previous case, ENDF/B-V files of the neutron total cross sections were used in the fitting program. A total of 16 isotope files were used (11 actinides and 5 fission products). The data were fit by calculating the total transmission from the product of the transmissions of the separate isotopes. The amount of each isotope was adjusted by finding the best fit for a prominent resonance of the isotope. Each isotope was then fit in succession and the process iterated until there was no change in the assigned abundance after several iterations. Results of the analysis are shown in Table II. In the paper reporting the work the fits and the residuals are shown for the complete spectra. There are a few resonances that were not identified and are left in the residuals, but aside from these, the residuals are consistent with the statistics.

In a subsequent paper we indicated how this technique could be applied to a complete nuclear fuel assembly using a small industrial linac with a low-Z target to supply neutrons. Figure 5 shows how such an installation might be arranged. The neutron transmission would be measured through the bundle of fuel rods.

Such a technique causes large variations in sample uniformity, but we have shown that sample inhomogeneity of a factor of ten can be made to cause no greater than a 1% error in the analysis.

The small PSPC was also used with a pinhole camera arrangement to image neutron distributions at the NBS Linac.

In the fall of 1979 it was apparent that it was not possible to obtain better resolution by using smaller PSPC detectors. Two programs were launched to develop two-dimensional detector systems that would have good resolution and, by eliminating the need for mechanical scanning, increase the efficiency and accuracy of the image generation.

In collaboration with M.K. Kopp of ORNL a program was initiated to develop a two-dimensional PSPC. A device was constructed with a sensitive area 5 cm x 5 cm. A resolution of about .9 mm was obtained, but the detector was difficult to use at the Linac because of instability induced by the intense gamma flash. However, this detector was used to image the 14 MeV neutron cone of the associated-particle system at the 3 MV Positive Ion Accelerator at NBS.

An alternate approach utilizing a microchannelplate (MCP) electron amplifier and a resistive-anode imaging system was also initiated. The device was made only 2.5 cm in diameter because of the great expense of larger units. Larger MCP systems are available- up to 7.5 cm in diameter- but for larger systems an anger camera approach would probably be more realistic.

The configuration of the NBS MCP detector system is shown in figure 6. The scale of the components has been distorted to show the method of operation. An incident neutron coming from the left interacts in the lithium glass scintillator. Light from the interaction causes electron emission at the photocathode. The electron current from the photocathode is amplified about a factor of 10 ^6 while its spatial distribution is maintained by the MCP. The centroid of the current distribution collected by the resistive anode indicates the coordinates of the initial neutron interaction. The resolution of the system is determined by the total number and the scattering of the photons that reach the photocathode. A small component of the overall resolution is caused by the 1% precision of centroid location inherent in the resistive-anode system.

Most of the work with this detector was done with a 0.5 mm thick scintillator of lithium glass containing 7.7% lithium enriched to 95% Li-6. For this thickness of scintillator the probability of neutron absorption in the glass is 4% at 10 eV.

The n,alpha reaction releases 4.8 MeV, which is absorbed within a volume of about 0.03 mm radius in the scintillator. From this volume, about 6700 photons are emitted isotropically, with a decay time of about 75 ns and a spectral distribution that peaks about 400 nm. The lithium glass scintillator is thus well suited to produce high-resolution images of short duration suitable for neutron time-of-flight radiography.

The light-scattering in the scintillator and the fibre-optic faceplate of the MCP are the major contributors to the resolution of the system. Resolution loss by light-scattering in the scintillator can be reduced by eliminating the photons reflected from the surface of the scintillator through which the neutrons enter. The fibre-optic lightpipe does not completely collimate the photons falling on its surface because the interface is not to air. Because of this refraction mismatch, about 76% of the photons are uncollimated.

To understand the resolution and efficiency of the MCP system,

a Monte Carlo program was written to simulate the system. Using this program, values of the expected resolution and efficiency were determined for a wide variety of models.

The intrinsic resolution of the MCP system was experimentally determined by a "knife edge" measurement with single photon counting. This measurement of the edge response function (ERF) verified the claimed .25 mm "electronic" resolution. The overall resolution of the system was determined by measuring the ERF for 4.9 eV neutrons using gold, and for neutrons below 0.03 eV using a cadmium, "knife edge". The results obtained in these two measurements were the same, indicating that neutron backscattering in the MCP did not seriously affect the resolution. Using the cadmium "knife edge," the resolution of the system and number of photons detected per incident neutron were measured for 0.5 and 1.0 mm thick scintillators, as well as with and without reflective backing. The results are shown in Table III.

These experimental results agreed within errors with the Monte Carlo results for the same conditions. The shape of the ERF obtained experimentally and that obtained from the Monte Carlo program are shown in figure 7 to agree quite well.

The best resolution obtained with the MCP system is about 0.75 mm FWHM. Monte Carlo calculations indicate that the photon-scattering component of the resolution could be reduced by a factor of two if the photon attenuation in the cladding glass of the fibre-optic light pipe were increased by a factor of ten. Another approach to improving the resolution would be to construct a MCP system in which the lithium glass was introduced into the MCP with the photocathode evaporated directly onto the lithium glass.

The great virtue of NRR is the ability to do multi-isotope imaging simultaneously. To illustrate this capacity, a sample was constructed of three elements: rhodium, tungsten, and gold. Letters 1 cm high were formed of the elements. The letters were then placed on top of one another and the x-ray image shown in figure 8 obtained. A NRR image of the sample was then made using the 1.26 eV resonance in rhodium, the 4.16 eV resonance in tungsten, and the 4.91 eV resonance in gold. The resulting images are shown in figure 9. The pixel size is .49 x .49 mm. Note the lack of interference between images.

The last application of NRR worked on at NBS was the measurement of small amounts of U-235 in simulated incinerator ash. Although NRR does not have the sensitivity of induced-activity techniques, it does offer the ability to determine the amount and position of any isotope in a complex matrix.

Powdered vermiculite of the appropriate density (0.23 g/cm^3) was used to simulate incinerator ash. A 2-liter bottle of vermiculite was inoculated with U-235 and the transmission spectrum measured using a He-3 linear PSPC and mechanical scanning to obtain two-dimensional coverage of the sample. Figure 10 shows an example of a fit to the spectral data. The smooth curve shown is the best fit to the 8.78 eV line at channel 220. These data were obtained with 10 g of U-235 mixed in the 2 liters of vermiculite and represents 2.1 x 10^-4 atoms/barn. The technique was tried with several different concentrations and containers ranging in size from the 2-liter container to a 55-gallon steel drum. Table IV shows a summary of the results. The observed accuracy is in good agreement with the accuracy that one would expect from simple analytic projections based on the area of the Breit-Wigner line. Although there are a number of drawbacks with this approach, the sensitivity to specific isotopes may make it useful in applications other than nuclear waste assay.

In summary, NRR offers a versatile technique having the unique capability to detect the amount and distribution of almost any isotope in a wide variety of conditions.

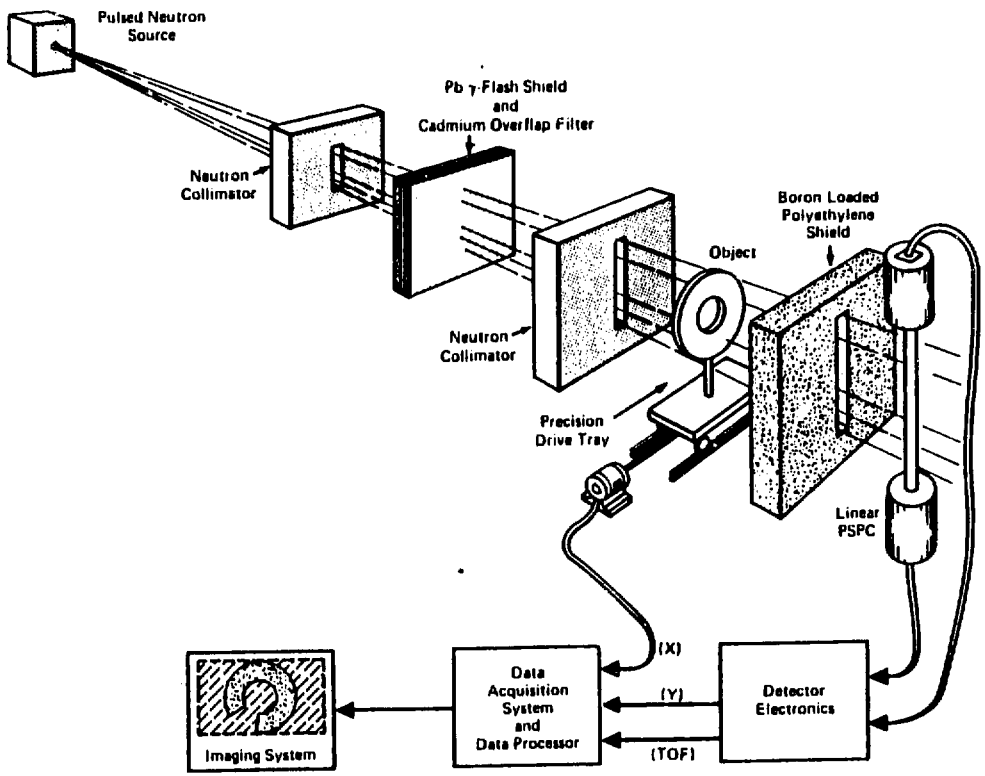

FIG. 1. Experimental Set Up

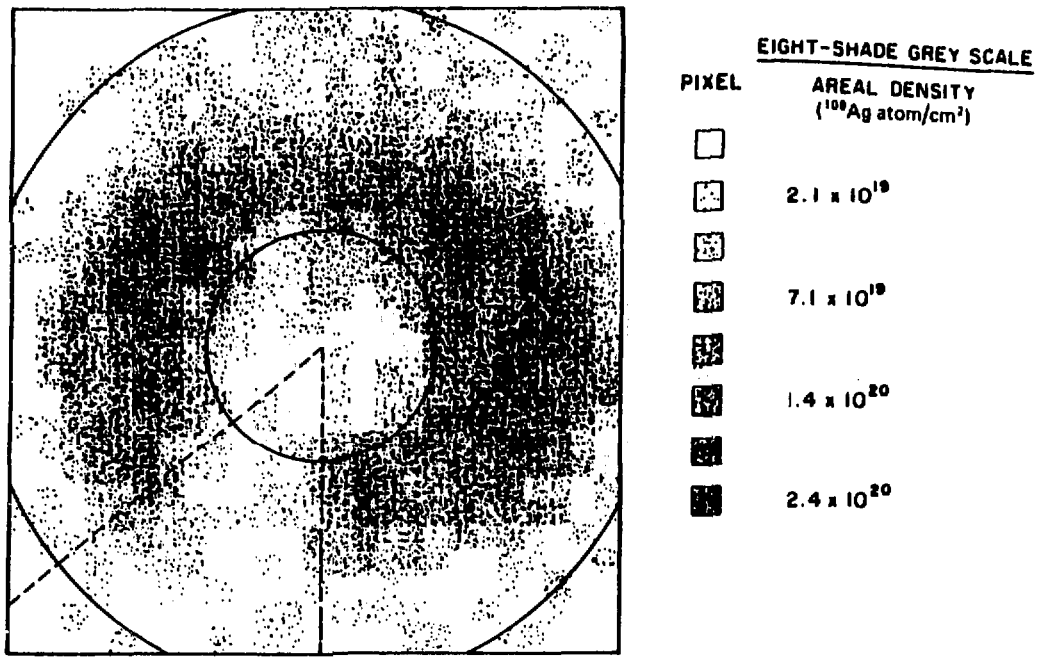

FIG. 2. PNR image from silver in test object.

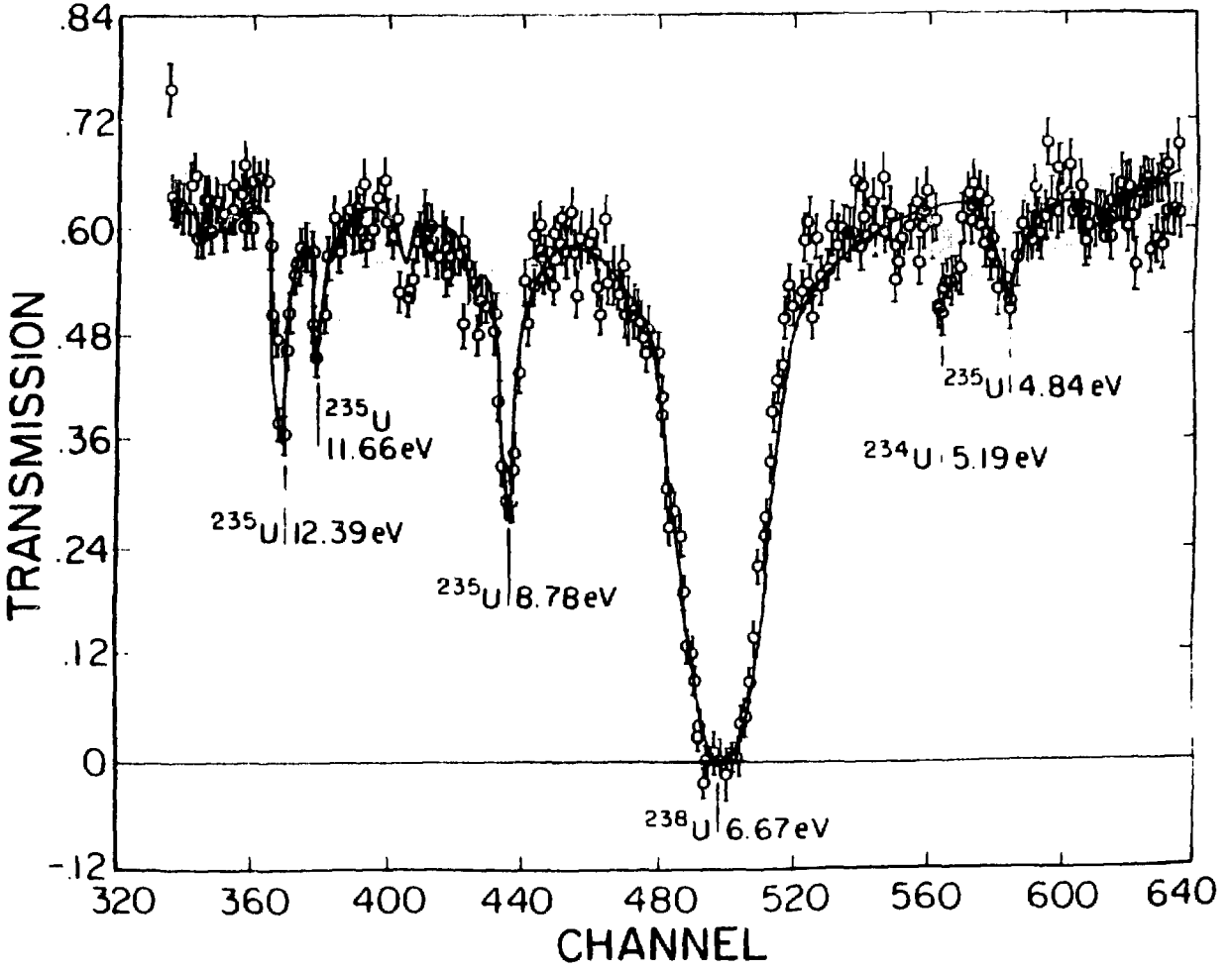

FIG. 3. Neutron transmission for nuclear fuel pellets.

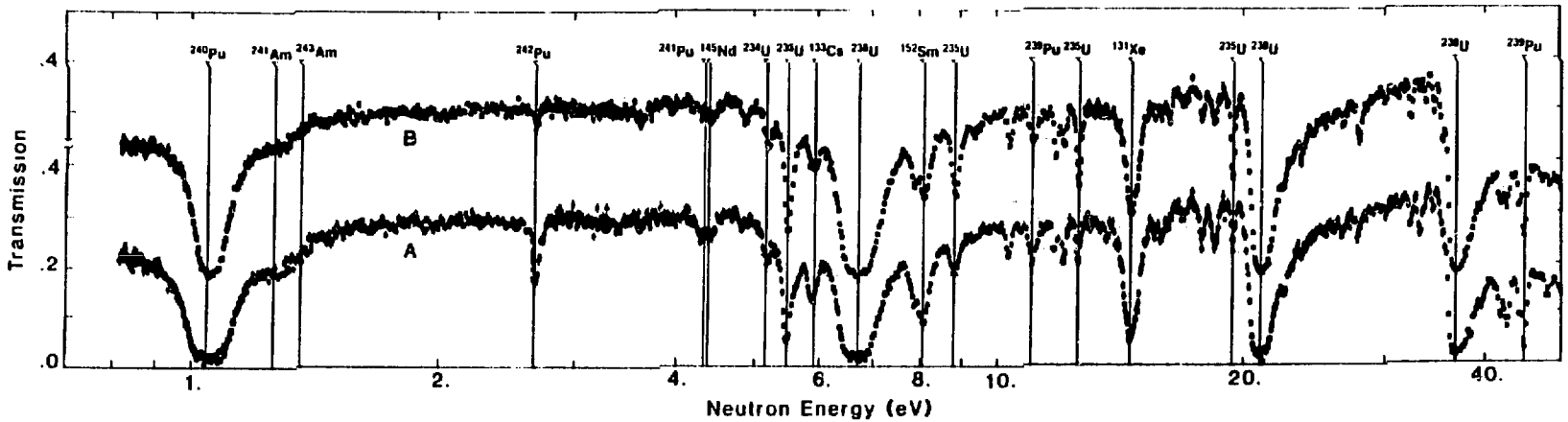

FIG. 4. Neutron transmission

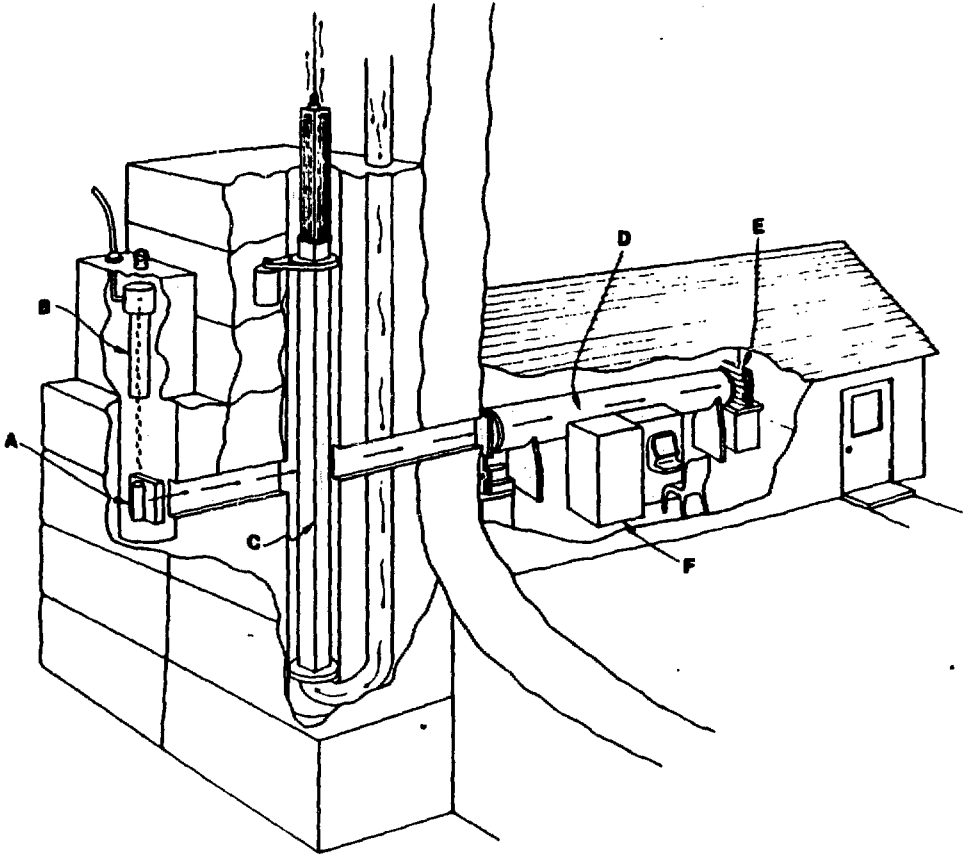

FIG. 5. Proposed set-up for nuclear fuel assaying.

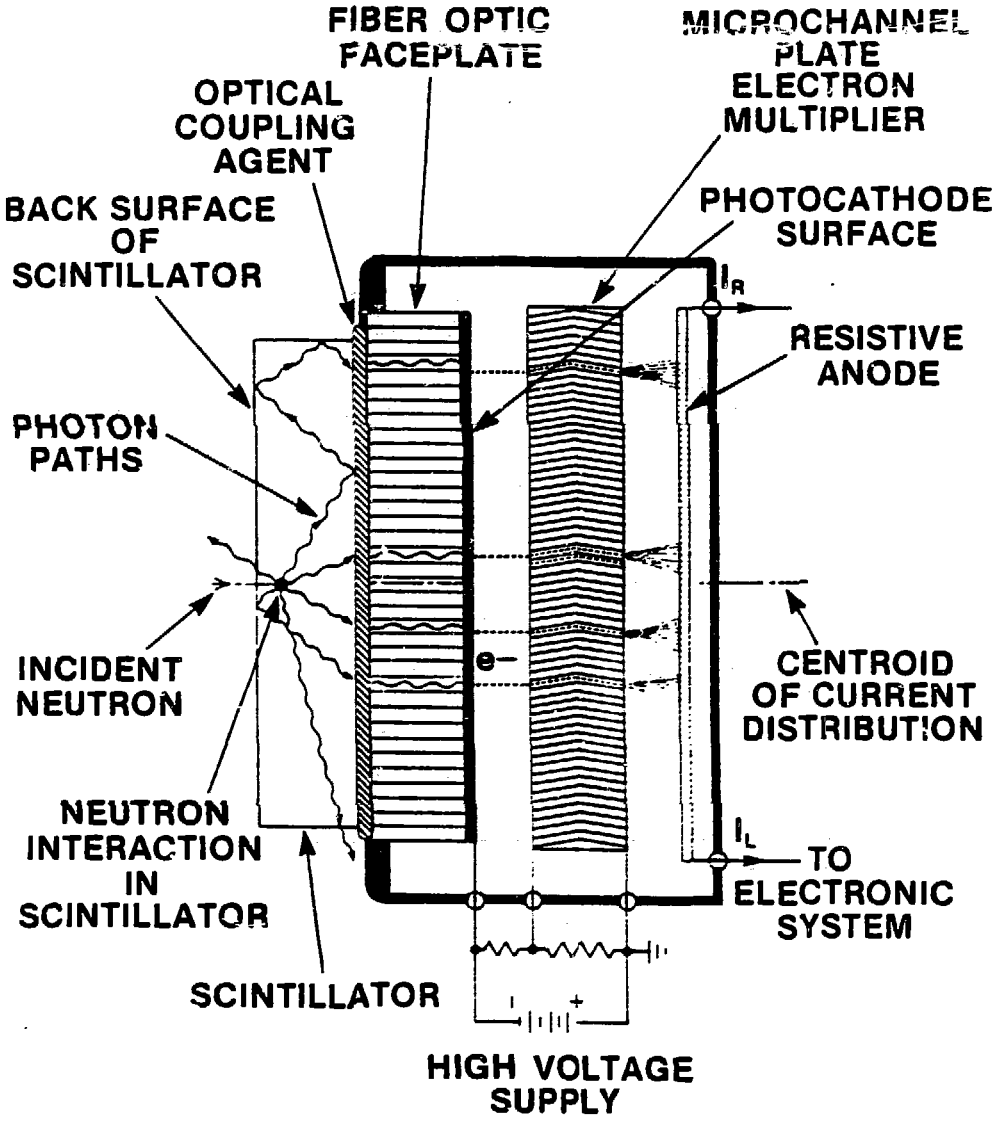

FIG. 6. Detector configuration

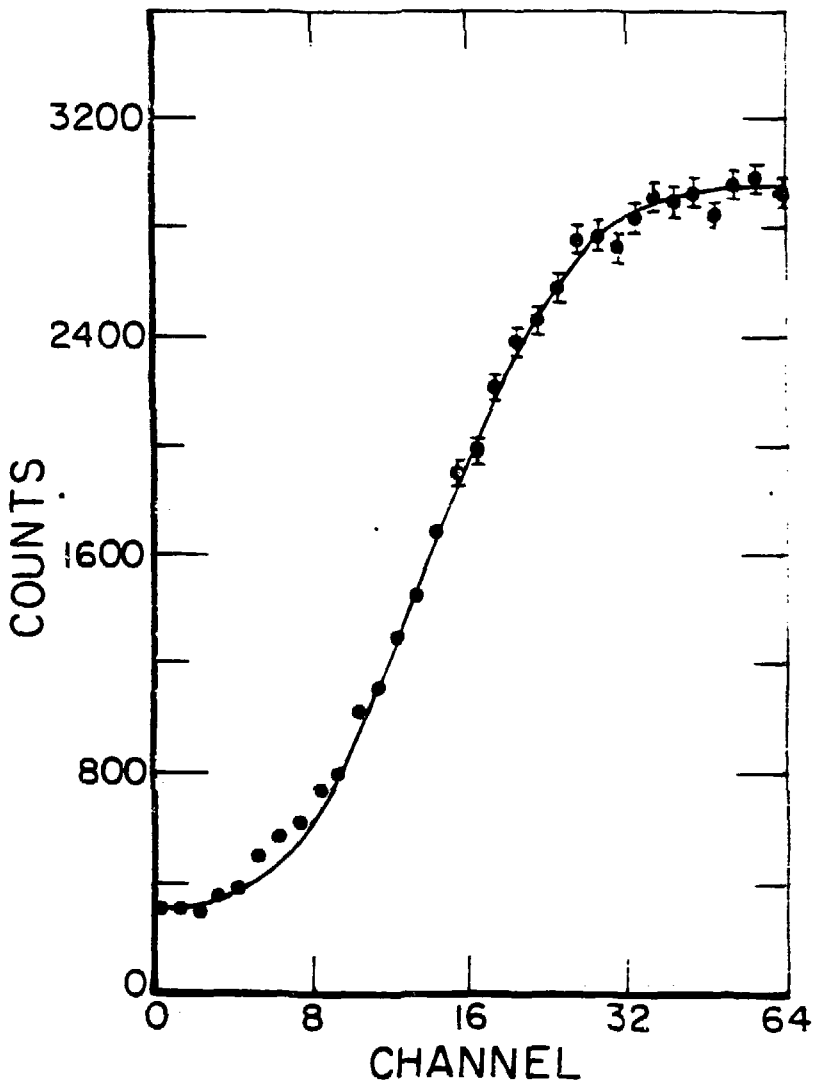

FIG. 7. Edge response function

FIG. 8. X-Ray Image

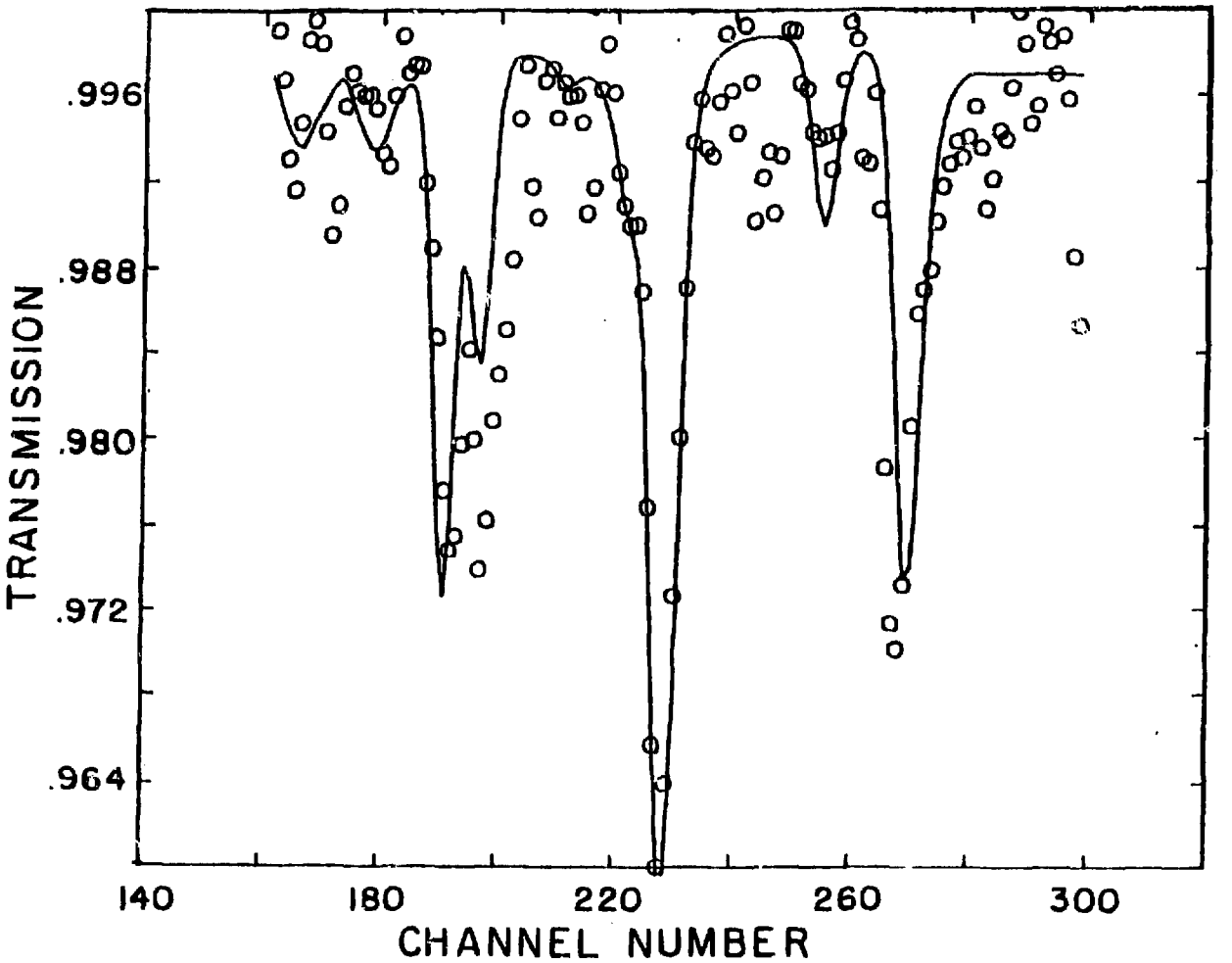

FIG. 10. Transmission of sample.

Table I

Abundance and Relative Abundance of ^{235}U and ^{238}U in Fresh Nuclear Fuel Samples

Sample	Isotope	Abundance (g/cm^2)	Relative Abundance[a] (%)	
			NRTA	Destructive Analysis
1	^{235}U	0.417 ± 0.005	4.01 ± 0.08	*3.96 ± 0.005*
	^{238}U	10.12 ± 0.15		
2	^{235}U	0.125 ± 0.018	1.10 ± 0.16	1.19 ± 0.005
	^{238}U	11.42 ± 0.12		

[a] 100 × atomic abundance of ^{235}U/total atomic abundance of uranium.

Table II

Isotope	Center Cut		End Cut	
	Abundance (atom/b) ($\times 10^{-5}$)	*Relative*[a] Abundance (%)	*Abundance* (atom/b) ($\times 10^{-5}$)	*Relative*[a] Abundance (%)
^{234}U	1.481 ± 0.060	0.03108	1.265 ± 0.038	0.02972
^{235}U	37.67 ± 0.85	0.7906	63.57 ± 0.65	1.494
^{236}U	15.79 ± 0.42	0.3314	9.12 ± 0.14	0.214
^{238}U	4765 ± 27	---	4256 ± 16	---
^{238}Pu	3.74 ± 0.76	0.0785	2.52 ± 0.43	0.0592
^{239}Pu	26.26 ± 0.60	0.5511	16.98 ± 0.36	0.3990
^{240}Pu	10.64 ± 0.15	0.2233	4.572 ± 0.043	0.1074
^{241}Pu	4.94 ± 0.33	0.104	1.37 ± 0.22	0.0322
^{242}Pu	1.512 ± 0.033	0.03173	0.202 ± 0.016	0.00474
^{131}Xe	3.382 ± 0.063	0.07098	1.595 ± 0.020	0.03748
^{133}Cs	7.63 ± 0.29	0.160	3.46 ± 0.19	0.0814
^{241}Am	5.52 ± 0.22	0.116	2.68 ± 0.13	0.0629
^{243}Am	0.705 ± 0.058	0.0148	0.197 ± 0.031	0.00463
^{152}Sm	0.694 ± 0.013	0.0146	0.3296 ± 0.0057	0.007744
^{145}Nd	3.096 ± 0.274	0.06497	1.67 ± 0.18	0.0392
^{99}Tc	9.94 ± 0.27	0.209	4.09 ± 0.19	0.0961

[a] 100 × atomic abundance of isotope/atomic abundance of ^{238}U.

Table III

Case	Scintillator back surface	Scintillator thickness (mm)	Fwhm of LRF (mm)	Adjusted $\bar{X}$	N_0
1	black	0.5	0.75 ± 0.10	0.46 ± 0.05	96 ± 10
2	white	0.5	0.84 ± 0.10	0.52 ± 0.05	192 ± 10
3	black	1.0	1.05 ± 0.10	0.34 ± 0.03	117 ± 12
4	white	1.0	1.20 ± 0.12	0.39 ± 0.04	207 ± 21

Table IV

Summary of Measurements

Container	Total Weight ^{235}U (g)	Effective Concentration (g/cm^3)	Effective Areal Density (g/cm^2)	atom/barn	Predicted Uncertainty (%)	Observed Uncertainty (%)	Absolute Error (%)
2 ℓ	0.958	4.8×10^{-4}	8.7×10^{-3}	2.2×10^{-5}	10	16	9.9
2 ℓ	2.901	1.5×10^{-3}	2.6×10^{-2}	6.7×10^{-5}	4.3	7.2	6.3
2 ℓ	9.219	4.6×10^{-3}	8.4×10^{-2}	2.1×10^{-4}	1.8	2.5	2.3
5 gal	9.219	8.0×10^{-4}	1.6×10^{-2}	4.1×10^{-5}	4.2	9.6	16
55 gal	9.219	3.2×10^{-4}	6.2×10^{-3}	1.6×10^{-5}	32	12	16